Linear Analysis of Melt Band Formation in a Mid-Ocean Ridge Corner Flow

D. J. Gebhardt and S. L. Butler
Department of Geological Sciences, University of Saskatchewan,
114 Science Place, Saskatoon, Saskatchewan, S7N 5E2, Canada

Key Points:

- Linear analysis of porosity band formation tests a potential mechanism for melt channeling at MORs
- Bands will favorably channel melt to the base of the plate instead of directly to the ridge axis
- The melt-channeling capacity of the bands is highly dependent on poorly constrained bulk viscosity

Abstract

Imposing external shear on systems of partial melt can cause compaction of the solid matrix and concentration of the interstitial liquid melt thereby generating bands of contrasting high and low porosity. These shear induced porosity bands have been proposed to channel melt beneath a mid-ocean ridge (MOR). In this contribution, we impose a shear flow that evolves as the bands are transported along streamlines of MOR corner flow. We evaluate the suitability of porosity band formation as a mechanism for melt channeling beneath a MOR using a linear instability analysis with three different matrix viscosity conditions: isotropic strain-rate independent, isotropic strain-rate dependent and anisotropic. Our analysis shows that the largest amplitude bands channel melt away from the ridge axis toward the base of the plate at the lithosphere-asthenosphere boundary while the effectiveness of channeling through the bands is highly dependent on the mantle bulk viscosity.

1. Introduction

While melt is extracted from mid ocean ridges within 1 km of the ridge axis [Vera et al, 1990], seismic evidence [Forsyth et al. 1998] indicates the presence of melt down to a depth of approximately 60 km in a broad region about 100 km wide. Additionally, geochemical evidence [Kelemen et al. 1997] points to rapid melt transport toward the extraction point at the ridge crest. However, the melt transport mechanism is still being debated. The numerical work of Richardson [1998] led to the suggestion that the formation of strain-induced porosity instabilities in partial melt could be a possible mechanism for melt extraction at MORs. Later numerical work [Katz et al., 2006, Katz, 2010] tested this prediction. The lateral melt channeling model of Katz et al. [2006] assumed that band orientation was rotated 25° retrograde to the background shear rotation from the compressive principle strain-rate direction based on the results of simple shear experiments [Holtzman et al., 2003, Holtzman and Kohlstedt, 2007, Kohlstedt et al. 2010, King et al., 2010] and strain-rate dependent models. A later MOR model by Katz [2010] used a temperature dependent, porosity-weakening, and strain-rate independent matrix viscosity and also included the effects of buoyancy. Under those circumstances, no bands formed in the MOR domain.

The present contribution differs from the approach utilized by Katz et al. [2006] in that instead of assuming a fixed orientation of the bands relative to the principle stress directions based on static simple shear results, we calculate the rotation and change in amplitude of bands

for a variety of initial orientations along MOR streamlines to determine the maximum perturbation amplitudes of bands as a function of their evolved angle. The present contribution also differs from the Katz [2010] model in that buoyancy and thermodynamics are neglected and three matrix viscosity models are tested: isotropic strain-rate independent, isotropic strain-rate dependent and anisotropic strain-rate independent matrix viscosity. In what follows, we will present further background information concerning shear induced melt bands in section 2, in section 3 we will present the linear theory used in our analysis, and finally, section 4 contains the results and discussion of our analysis.

2. Shear Induced Melt Bands

Partial melt porosity instabilities have been the subject of extensive experimental and numerical investigation. Defined as the band-like regions of concentrated and depleted melt fraction, these instabilities have been found to exist in a variety of experimental flow geometries [Holtzman et al., 2003, Holtzman and Kohlstedt, 2007, Kohlstedt et al. 2010, Qi et al, 2015] for both Newtonian and non-Newtonian rheology regimes [King et al., 2010]. Bands formed during experiments were found to be oriented approximately 20° from the shear plane and approximately 25° from the direction of maximum compression.

Early theoretical work identified porosity-weakening matrix viscosity as a necessary factor in shear-induced melt localization [Stevenson, 1989]. Solutions for Newtonian rheology models saw bands grow fastest parallel to the direction of maximum compression, or 45° from the shear plane [Spiegelman, 2003]. Introducing strain-rate dependence to the matrix viscosity saw bands favor an orientation of about 15°-20° from the shear plane, but only for very high strain-rate dependence outside the accepted range for mantle materials [Katz et al., 2006, Butler, 2009]. Most recently, an anisotropic matrix viscosity model has been proposed [Takei and Holtzman, 2009, Takei and Katz, 2013], introducing an anisotropic viscosity tensor that couples the shear and volumetric components of the matrix stress/strain rate. This model accounts for a preferential alignment of melt pockets along grain boundaries in two-phase systems under stress [Takei and Katz, 2013, Daines and Kohlstedt, 1997]. Application of this new viscosity model in numerical simulations by Butler [2012] and Katz and Takei [2013] saw low angle bands form; however, these low angle bands do not persist for anisotropy models that are consistent with the experimental observations of melt pockets at high strains [Holtzman and Kohlstedt, 2007].

3. Theory

The equations governing compacting two-phase systems were derived by McKenzie [1984] and Scott and Stevenson [1984]. In those contributions, the presented equations described the movement of both the melt and matrix phases in a system of partial melt in terms of force and mass balances. We use the nondimensionalized form of these force and mass balance equations found in Butler [2010]. We employ a matrix permeability defined by $k_\phi = \left(\frac{\phi}{\phi_0}\right)^3$ [Carmen, 1939]. The porosity and strain-rate dependent matrix viscosity used in this contribution is the same porosity and strain-rate weakening law as found in Butler [2009, 2010] and Katz et al. [2006] and it is given by:

$$\eta = exp\left(\frac{\alpha(\phi-\phi_0)}{n_v}\right)\left[\frac{1}{\sqrt{2}}\left[\frac{dU}{dx}^2 + \frac{dV}{dy}^2 + \frac{1}{2}\left(\frac{dU}{dy}+\frac{dV}{dx}\right)^2\right]^{0.5}\right]^{\frac{(1-n_v)}{n_v}} \quad (1)$$

where $\alpha = -25$ [Mei et al, 2002]. Newtonian viscosity is achieved by setting the strain-rate exponent, n_v, to 1 while $n_v \neq 1$ yields non-Newtonian viscosities corresponding to different creep regimes for mantle materials [Korenaga and Karato, 2008, Hirth and Kohlstedt, 2003]. U and V are the horizontal and vertical components of the velocity field for the matrix phase, ϕ_0 is the initial background porosity and ϕ is the porosity. The partial derivatives of U and V are the components of the strain-rate tensor. Each of these strain rate components consist of zeroth and first order terms, describing the background MOR corner flow strain-rate and a variation from the background strain-rate, respectively.

The anisotropic viscosity model we use comes from Takei and Katz [2013], which is a generalized version of a previous model from Takei and Holtzman [2009]. It is centered on the introduction of an anisotropy tensor, which includes an anisotropy angle and a magnitude as parameters. Following Takei and Katz [2013], the angle is defined to be the local direction of maximum tensile stress. The magnitude is defined as

$$\alpha = 2\tanh\left(\frac{2(\sigma_3-\sigma_1)}{\sigma_{sat}}\right), \quad (2)$$

where $\sigma_1, \sigma_3, \sigma_{sat}$ are the principle compression, principle tension and the saturation stress, respectively. The saturation stress is defined as a material property, and is taken to be 2 as in Takei and Katz [2013] where stress is made dimensionless by the background viscosity and strain-rate.

For the background flow, we use isoviscous corner flow [Spiegelman and McKenzie, 1987, Batchelor, 1967] for which streamlines are shown in Figure 1. Slow spreading ridges have

wedge angles of approximately 40° [Spiegelman and McKenzie, 1987]. Figure 1b contains the same ridge geometry, but shows the variation of the orientation of the strain-rate axes of tension (red) and compression (black) with position. Previous work with compacting systems has shown that these directions are very important, as porosity bands tend to form at angles relative to the angle of maximum compression, and as the main components of the anisotropic viscosity model are dependent on the directions of maximum tension and maximum compression. The principle axes in Figure 1b are similar to the axes for highly strain-rate and temperature dependent matrix viscosity [Katz et al, 2006]. Takei and Holtzman [2009] also used the isoviscous corner flow in models of the fluid pressure gradients at MORs.

In the perturbation analysis, the porosity field is decomposed into plane waves [Spiegelman, 2003] of the form:

$$\phi = \phi_0 + \Delta\phi exp\left(i\left(k_x(t)x + k_y(t)y\right) + s(t)\right). \quad (3)$$

All of the first order perturbations of the other dynamical variables are assumed to be proportional to the ϕ perturbation. In equation (3), $\Delta\phi$ corresponds to the initial porosity perturbation amplitude, $k_x(t)$ and $k_y(t)$ correspond to orientation-defining wavenumbers in the x and y directions and $s(t)$ corresponds to the amplitude of the porosity perturbation. The time derivative of the amplitude is the growth rate of the porosity perturbation.

The wavenumbers are considered to be time dependent just as in the linear analysis of Spiegelman [2003]. However because the mid-ocean ridge produces a shear with both simple and pure components, this contribution uses more general evolution equations for the wavenumbers [Craik and Criminale, 1986] given by:

$$\frac{dk_x}{dt} = -\frac{dU_b}{dx}k_x - \frac{dV_b}{dx}k_y, \quad (4)$$

$$\frac{dk_y}{dt} = -\frac{dU_b}{dy}k_x - \frac{dV_b}{dy}k_y. \quad (5)$$

Equations (4) and (5) describe the rotation of the bands by the background flow; in them, U_b and V_b are the background horizontal and vertical velocity components, respectively. The multi-component shear of the corner flow also leads to a growth rate that is different than that found in previous contributions. Only linear variations of the background velocity are taken into account in our analysis. This approximation is valid provided that the modeled fluid parcels are much smaller than the length scale of the MOR domain over which the flow is changing.

The method used to derive the growth rate is very similar to the method used by Butler [2012]. The Fourier transform of the nondimensionalized, first-order-perturbed force and mass balance equations for systems of partial melt are expressed in the form of matrix-vector multiplication. The matrix is then inverted to solve for the transformed horizontal and vertical velocity components and pressure. The coefficients indicating the amplitude of the horizontal and vertical velocity perturbation components relative to the porosity perturbation amplitude, $\widetilde{U}$ and $\widetilde{V}$, are then substituted into the equation for the growth rate, which is derived from the mass conservation equation for the solid phase and is given by:

$$\frac{ds}{dt} = (1-\phi_0)\left(ik_x\widetilde{U} + ik_y\widetilde{V}\right). \quad (6)$$

Equations (4), (5), (6), along with equations defining the mid-ocean ridge streamlines [Spiegelman and McKenzie, 1987] serve as the basis of the linear analysis of this contribution. The equations are solved simultaneously using an ODE solver in Matlab along multiple streamlines that increase in distance from the ridge axis. Each streamline is started at a depth of 70 km and ends at the lithosphere-asthenosphere boundary, which is a depth location that increases with increasing distance from the ridge axis (see Fig. 1). Band orientation can be expressed in terms of angle by making the substitution $k_x = |k|sin\theta$ and $k_y = |k|cos\theta$, where θ is defined as the clockwise angle from the positive horizontal axis. The center of the calculation domain translates along the MOR streamlines while the coordinate system maintains a fixed orientation. Bands were evolved for initial angles in the range $\theta\epsilon[0,\pi]$. We imposed a unit amplitude initial condition by setting $s(0) = 0$.

4. Results and Discussion

Examples of growth rates from two different positions in the slow spreading MOR domain are shown in Figures 2a and 2b. Previous studies have shown that multiple growth rate maxima are expected for both the strain-rate dependent and anisotropic rheologies [Katz et al., 2006, Butler, 2009, Takei and Katz, 2013]. Figure 2a demonstrates the near-isotropic (α=0.29), strain-rate independent behavior of the anisotropic viscosity at 1km from the ridge axis at a depth of 50km. The anisotropic growth rate curve in Figure 2b at 40km from the ridge axis at a depth of 50 km shows two distinct maxima. The peaks in Figures 2a and 2b demonstrate an angular shift of about 50°, resulting from the difference in the flow geometries at the two locations. The angles along the x-axis correspond to clockwise-positive orientations in the range $[0,\pi]$. At each point along streamlines in the MOR domain, equation (5) is evaluated at each angle in this range.

This enables expressing the growth rate and its maxima as a function of an instantaneous orientation relative to horizontal. When selecting maximum growth rate orientations in cases where more than one peak is present in the growth rate, the local maxima corresponding to the lower of two angles was selected. The reason for this selection relates to the background vorticity, which is clockwise throughout the entire MOR domain. In the local reference frame defining the orientation of the porosity bands, the higher angle maxima will then be rotated over time by the background flow to decaying amplitude orientations. This is consistent with previous studies that use simple shear, which have shown background flows quickly rotating high angle bands away from orientations with positive growth rates while low angle bands remain in favorable orientation for perturbation growth [Katz et al., 2006].

Figure 3 presents contour plots of the maximum growth rate throughout the MOR domain with corresponding band orientations overlain as white bars for positions along multiple streamlines. Figure 3a clearly demonstrates that for isotropic, strain-rate independent viscosity, the maximum instantaneous growth rate orientations are parallel to the direction of maximum compression (the black lines in Figure 1b), as predicted by theory. The isotropic, strongly strain-rate dependent ($n_v = 6$) bands with maximum growth rate in Figure 3b demonstrate orientations at consistently low angles to the direction of maximum compression throughout the MOR domain. In certain locations in the sub MOR mantle, this results in preferential orientations toward the ridge axis, in agreement with Katz et al. [2006]. The maximum growth rate bands corresponding to anisotropic matrix viscosity in Figure 3c demonstrate a range of orientations. This orientation range is attributed to the anisotropy magnitude defined by equation (2). Close to the ridge axis where shear is low, the anisotropy magnitude tends to 0, which corresponds to isotropic viscosity. It is not until farther away from the ridge axis, where shear is greater, that the anisotropy magnitude is close enough to its defined maximum value of 2 that the bands occur at low angles to the direction of maximum compression.

The contour plots in Figure 4 show the maximum perturbation amplitude throughout the MOR domain with corresponding evolved band orientations overlain as white bars for positions along multiple streamlines. In both the case of strain-rate dependent and anisotropic viscosity, multiple orientations for the maximum perturbation amplitude are plotted when the magnitude of a second distinct maximum is within 10% of the greatest perturbation amplitude. Where only a single orientation is given, the second peak has been absorbed into the first leading to a very

broad single peak. The half-maximum envelope is therefore indicated by the green bars in all of the perturbation amplitude plots to demonstrate the potential angular range of both the very broad single peaks and the multiple peaks present. Comparing the corresponding viscosity cases in Figures 3 and 4, it is clear that the bands with the largest amplitude are rotated clockwise from the orientation of fastest growth. The magnitude of the band rotation depends on the relative sizes of the vorticity of the background flow and growth rate of the perturbation. Knowing this, the results shown in Figure 4 demonstrate the significant influence of the background flow: the maximally perturbed bands for all three rheologies have been rotated by the background flow away from the maximum growth rate orientation, resulting in bands directed toward the base of the plate at the lithosphere-asthenosphere boundary. This analysis was also completed using a fast spreading ridge geometry (wedge angle of 13°), the results of which were qualitatively similar. This is because the fluid parcel travel time decreases for fast spreading ridges while the integrated strain is similar in both ridge geometries.

The linear analysis presented here will possibly only be strictly valid close to the fixed initial condition $\phi_0 = 0.01$. However, previous work by Butler [2009, 2010] has shown good agreement between the results of linear and nonlinear models up to strains of around 1. A further limitation is placed on this analysis in the form of two poorly constrained physical quantities, the initial perturbation amplitude, $\Delta\phi$, and the matrix bulk viscosity. Porosity in the mantle can have values in the range [0,0.3], where 0.3 corresponds to the rheologically critical melt fraction (RCMF), the point at which contiguity between grains is lost [Scott and Kohlstedt, 2006]. In order for the porosity to not become less than 0 locally, a maximum value of $s_{max} = \ln(\frac{\phi_0}{\Delta\phi})$ can be determined from equation (3) by setting $\phi = 0$ and the oscillatory part of the exponential to -1. Another boundary for the perturbation amplitude is required to keep the local porosity less than the RCMF, but since our initial porosity is fixed in this analysis at 1%, the lower bound is our greater concern. A lack of constraint on $\Delta\phi$ leads to variability in the value of s_{max}. For example when $\Delta\phi = 0.1\phi_0$, $s_{max} = 6.8977$while for $\Delta\phi = 0.0001\phi_0$, $s_{max} = 9.2103$. The results in Figure 4 are plotted using $\Delta\phi = 0.1\phi_0$. It is clear that for the Newtonian viscosity case the amplitude exceeds s_{max}in much of the domain, however for both the non-Newtonian viscosity and anisotropic viscosity in Figure 4b and 4c, respectively, the porosity results are valid for a larger portion of the MOR domain.

The lack of constraint on $\Delta\phi$ also affects predictions for the variation in permeability throughout the MOR domain. The region with the highest permeability variation is generally located along the lithosphere-asthenosphere boundary, though the vertical extent of this region is variable. The permeability range decreases with decreasing $\Delta\phi$, and therefore decreasing the range in permeability would result in less effective channeling through the bands. When $\Delta\phi = 0.1\phi_0$, the permeability increases by a factor of 10^4 from the starting depth to the base of the plate, with large increases in permeability already present at depths of around 30km below the base of the plate. For $\Delta\phi = 0.0001\phi_0$, the permeability varies by only a factor of 10^{-2} in the whole MOR domain and the highest permeability is confined right along the base of the plate. Therefore for the small values of $\Delta\phi$ required to make all the cases of the linear analysis presented here valid, channeling through bands would likely only be effective very close to the base of the plate, although effective channeling could occur at a greater depth for the strain-rate dependent and anisotropic viscosity bands due to the range in acceptable values of $\Delta\phi$.

The presented results use a bulk viscosity that is 5/3 the shear viscosity [Takei and Katz, 2013]. The analysis was repeated with an increased bulk viscosity of 200, consistent with other theoretical models where the bulk viscosity varies inversely with porosity [Bercovici and Ricard, 2003]. This increase resulted in a decrease in magnitude for both the growth rate and perturbation amplitude with little effect on orientation for all viscosity cases. Increasing the bulk viscosity also results in a significant decrease in the range of permeability. When $\Delta\phi = 0.1\phi_0$, the permeability increases by only a factor of 10^{-2} while for $\Delta\phi = 0.0001\phi_0$, the permeability varies by a factor of 10^{-5}. The significance of the melt bands both in terms of amplitude and channeling ability is therefore greatly reduced in the presence of a greatly increased bulk viscosity.

5. Conclusions

This contribution has demonstrated that the fastest growing porosity perturbations can be oriented favorably for channeling melt directly to the ridge axis for both highly strain-rate dependent and anisotropic matrix viscosities. However, this favorable instantaneous angle is not preserved over time as bands calculated with all three rheology laws corresponding to the greatest perturbation amplitude are oriented more favorably for channeling melt toward the base of the plate at the lithosphere-asthenosphere boundary. The bands presented here have sufficient amplitude to channel melt only for low values of bulk viscosity, and depending on the initial

perturbation amplitude, the bands may only be significant close to the base of the plate. Melt channeled along bands toward the base of the plate is in keeping with the theoretical melt transport model proposed by Sparks and Parmentier [1991]. In this model, the authors address lateral melt transport with the claim that upwelling partial melt from the mantle freezes along the impermeable lithosphere-asthenosphere boundary. This freezing results in the formation of a high porosity decompaction boundary layer, where melt could be transported toward the ridge axis under the influence of gravity along the base of the plate.

Future considerations will incorporate the corner flow into a fully nonlinear model, as well as include the effects of buoyancy and thermodynamics. Butler [2009] demonstrated that buoyancy can play a significant role in allowing bands to remain close to the fastest growth-rate orientation, which contrasts the lack of porosity band formation seen in the MOR models of Katz [2010] that incorporated buoyancy. Thermodynamics can be introduced through the inclusion of ongoing melting and the addition of temperature dependence to the viscosity of both the solid matrix and the background flow.

6. Acknowledgments

We are grateful to Richard Katz and an anonymous reviewer for their helpful comments that greatly improved this manuscript. The authors are grateful for funding received through NSERC. The authors declare no conflicts of interest.

7. References

Batchelor, G. (1967), *An introduction to fluid dynamics*, U.P., Cambridge.

Bercovici, D., and Y. Ricard (2003), Energetics of a two-phase model of lithospheric damage, shear localization and plate-boundary formation, *Geophysical Journal International*, *152*(3), 581-596, doi:10.1046/j.1365-246x.2003.01854.x.

Butler, S. L. (2009), The effects of buoyancy on shear-induced melt bands in a compacting porous medium, *Physics of the Earth and Planetary Interiors*, *173*(1-2), 51-59, doi:10.1016/j.pepi.2008.10.022.

Butler, S. L. (2010), Porosity localizing instability in a compacting porous layer in a pure shear flow and the evolution of porosity band wavelength, *Physics of the Earth and Planetary Interiors*, *182*(1-2), 30-41, doi:10.1016/j.pepi.2010.06.004.

Butler, S. L. (2012), Numerical models of shear-induced melt band formation with anisotropic matrix viscosity, *Physics of the Earth and Planetary Interiors*, *200-201*, 28-36, doi:10.1016/j.pepi.2012.03.011.

Carman, P. (1939), Permeability of saturated sands, soils and clays, *J. Agric. Sci.*, *29*(02), 262, doi:10.1017/s0021859600051789.

Craik, A., and W. Criminale (1986), Evolution of Wavelike Disturbances in Shear Flows: A Class of Exact Solutions of the Navier-Stokes Equations, *Proceedings of the Royal Society A: Mathematical, Physical and Engineering Sciences*, *406*(1830), 13-26, doi:10.1098/rspa.1986.0061.

Daines, M., and D. Kohlstedt (1997), Influence of deformation on melt topology in peridotites, *J.*

309 *Geophys. Res.*, *102*(B5), 10257, doi:10.1029/97jb00393.
310 Forsynth, D., D.S. Sheirer, S.C. Webb, et al (1998), Imaging the Deep Seismic Structure Beneath
311 a Mid-Ocean Ridge: The MELT Experiment, *Science*, *280*(5367), 1215-1218,
312 doi:10.1126/science.280.5367.1215.
313 Hirth, G., and D. Kohlstedt (2003), Rheology of the upper mantle and the mantle wedge: A view
314 from the experimentalists, *Inside the Subduction Factory*, 83-105, doi:10.1029/138gm06.
315 Holtzman, B., and D. Kohlstedt (2007), Stress-driven Melt Segregation and Strain Partitioning in
316 Partially Molten Rocks: Effects of Stress and Strain, *Journal of Petrology*, *48*(12), 2379-
317 2406, doi:10.1093/petrology/egm065.
318 Holtzman, B., N. Groebner, M. Zimmerman, S. Ginsberg, and D. Kohlstedt (2003), Stress-driven
319 melt segregation in partially molten rocks, *Geochemistry, Geophysics, Geosystems*, *4*(5),
320 n/a-n/a, doi:10.1029/2001gc000258.
321 Katz, R., M. Spiegelman, and B. Holtzman (2006), The dynamics of melt and shear localization
322 in partially molten aggregates, *Nature*, *442*(7103), 676-679, doi:10.1038/nature05039.
323 Katz, R. (2010), Porosity-driven convection and asymmetry beneath mid-ocean ridges,
324 *Geochemistry, Geophysics, Geosystems*, *11*(11), n/a-n/a, doi:10.1029/2010gc003282.
325 Katz, R., and Y. Takei (2013), Consequences of viscous anisotropy in a deforming, two-phase
326 aggregate. Part 2. Numerical solutions of the full equations, *J. Fluid Mech.*, *734*, 456-485,
327 doi:10.1017/jfm.2013.483.
328 Kelemen, P., G. Hirth, N. Shimizu, M. Spiegelman, and H. Dick (1997), A review of melt
329 migration processes in the adiabatically upwelling mantle beneath oceanic spreading ridges,
330 *Philosophical Transactions of the Royal Society A: Mathematical, Physical and*
331 *Engineering Sciences*, *355*(1723), 283-318, doi:10.1098/rsta.1997.0010.
332 King, D., M. Zimmerman, and D. Kohlstedt (2010), Stress-driven Melt Segregation in Partially
333 Molten Olivine-rich Rocks Deformed in Torsion, *Journal of Petrology*, *51*(1-2), 21-42,
334 doi:10.1093/petrology/egp062.
335 Kohlstedt, D., M. Zimmerman, and S. Mackwell (2010), Stress-driven Melt Segregation in
336 Partially Molten Feldspathic Rocks, *Journal of Petrology*, *51*(1-2), 9-19,
337 doi:10.1093/petrology/egp043.
338 Korenaga, J., and S. Karato (2008), A new analysis of experimental data on olivine rheology, *J.*
339 *Geophys. Res.*, *113*(B2), doi:10.1029/2007jb005100.
340 McKenzie, D. (1984), The Generation and Compaction of Partially Molten Rock, *Journal of*
341 *Petrology*, *25*(3), 713-765, doi:10.1093/petrology/25.3.713.
342 Mei, S., W. Bai, T. Hiraga, and D. Kohlstedt (2002), Influence of melt on the creep behavior of
343 olivine-basalt aggregates under hydrous conditions, *Earth and Planetary Science Letters*,
344 *201*(3-4), 491-507, doi:10.1016/s0012-821x(02)00745-8.
345 Qi, C., D. Kohlstedt, R. Katz, and Y. Takei (2015), Experimental test of the viscous anisotropy
346 hypothesis for partially molten rocks, *Proceedings of the National Academy of Sciences*,
347 201513790, doi:10.1073/pnas.1513790112.
348 Richardson, C. (1998), Melt flow in a variable viscosity matrix, *Geophys. Res. Lett.*, *25*(7), 1099-
349 1102, doi:10.1029/98gl50565.
350 Scott, D., and D. Stevenson (1984), Magma solitons, *Geophys. Res. Lett.*, *11*(11), 1161-1164,
351 doi:10.1029/gl011i011p01161.
352 Scott, T., and D. Kohlstedt (2006), The effect of large melt fraction on the deformation behavior
353 of peridotite, *Earth and Planetary Science Letters*, *246*(3-4), 177-187,
354 doi:10.1016/j.epsl.2006.04.027.
355 Sparks, D., and E. Parmentier (1991), Melt extraction from the mantle beneath spreading centers,

Earth and Planetary Science Letters, *105*(4), 368-377, doi:10.1016/0012-821x(91)90178-k.
Spiegelman, M., and D. McKenzie (1987), Simple 2-D models for melt extraction at mid-ocean ridges and island arcs, *Earth and Planetary Science Letters*, *83*(1-4), 137-152, doi:10.1016/0012-821x(87)90057-4.
Spiegelman, M. (2003), Linear analysis of melt band formation by simple shear, *Geochemistry, Geophysics, Geosystems*, *4*(9), n/a-n/a, doi:10.1029/2002gc000499.
Stevenson, D. (1989), Spontaneous small-scale melt segregation in partial melts undergoing deformation, *Geophys. Res. Lett.*, *16*(9), 1067-1070, doi:10.1029/gl016i009p01067.
Takei, Y., and B. Holtzman (2009), Viscous constitutive relations of solid-liquid composites in terms of grain boundary contiguity: 3. Causes and consequences of viscous anisotropy, *J. Geophys. Res.*, *114*(B6), doi:10.1029/2008jb005852.
Takei, Y., and R. Katz (2013), Consequences of viscous anisotropy in a deforming, two-phase aggregate. Part 1. Governing equations and linearized analysis, *J. Fluid Mech.*, *734*, 424-455, doi:10.1017/jfm.2013.482.
Vera, E., J. Mutter, P. Buhl, J. Orcutt, A. Harding, M. Kappus, R. Detrick, and T. Brocher (1990), The structure of 0- to 0.2-m.y.-old oceanic crust at 9°N on the East Pacific Rise from expanded spread profiles, *J. Geophys. Res.*, *95*(B10), 15529, doi:10.1029/jb095ib10p15529.

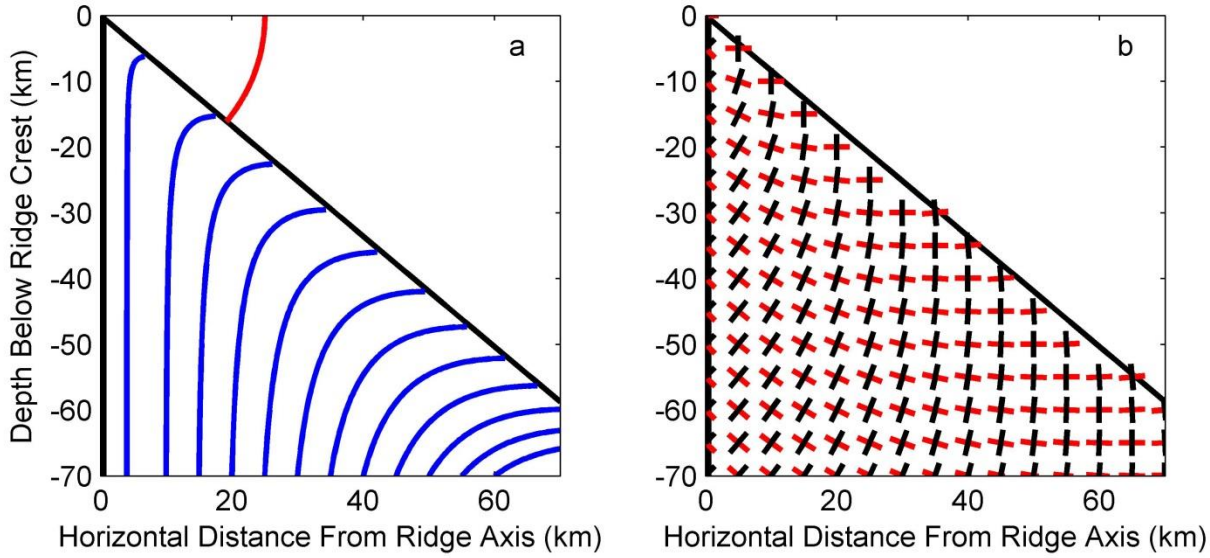

Figure 1: MOR geometry. a) Blue lines denote the corner flow streamlines. The lithosphere-asthenosphere boundary is given by the inclined black line, while the vertical black line represents the axis of symmetry for the ridge, with the origin being the ridge axis. The angle between the lithosphere-asthenosphere boundary and horizontal, given by the red curve, defines the wedge angle. b) Direction of maximum compression (black) and maximum tension (red) for the MOR domain.

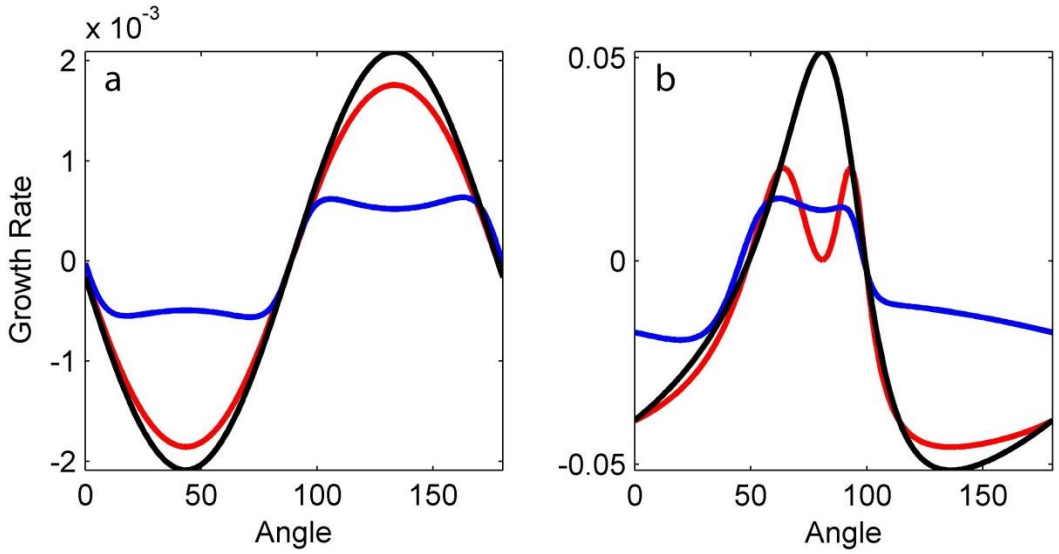

Figure 2: Growth rate variation with orientation. Strain-rate independent (black), strain-rate dependent (blue), and anisotropic viscosities (red) are plotted for (a) 1 km from the ridge axis and (b) 40 km from the ridge axis, all at a depth of 50 km.

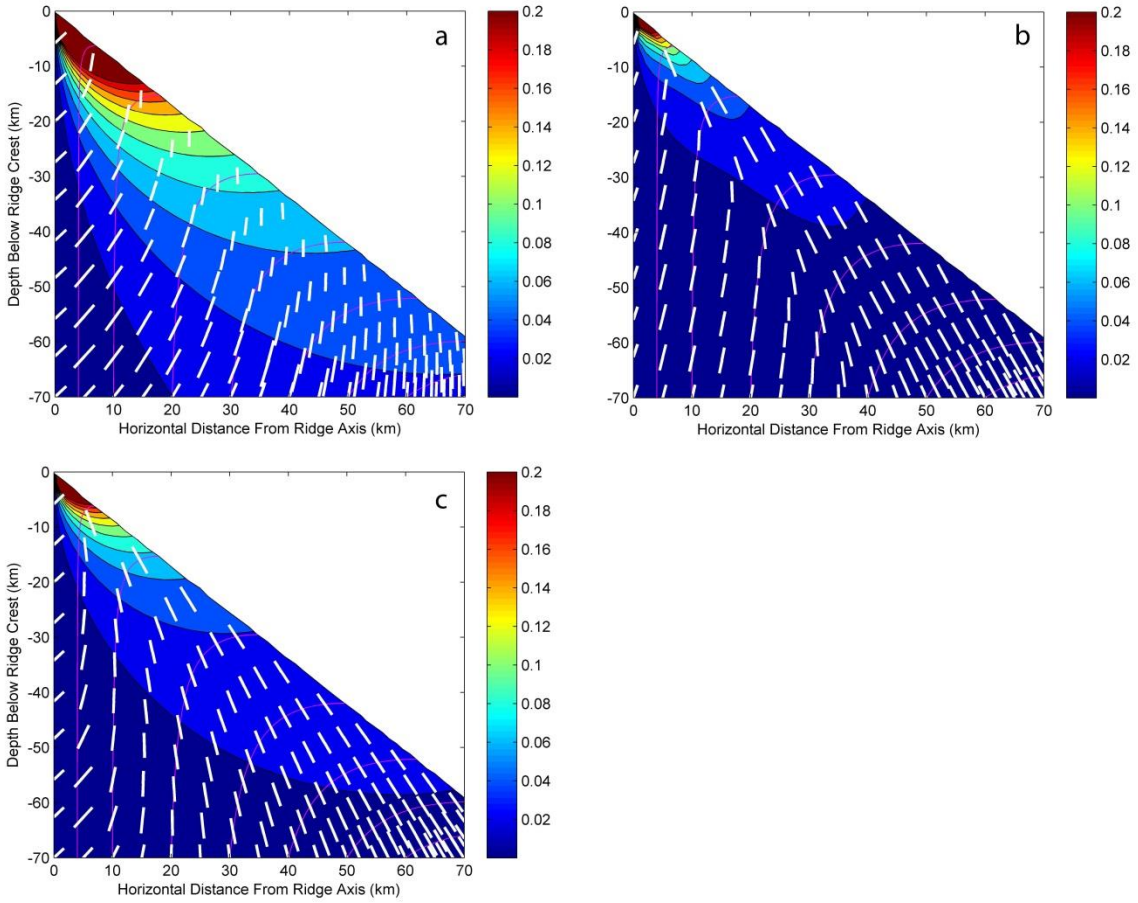

Figure 3: Contour plots of maximum instantaneous growth rate with corresponding orientations given in white. a) Bands corresponding to isotropic strain-rate independent rheology are oriented mostly toward the lithosphere-asthenosphere boundary. b) For bands with isotropic strain-rate dependent rheology, orientations are consistently at low angles to the direction of maximum compression resulting in regions where bands are oriented toward the ridge axis. c) Anisotropic strain-rate independent bands are also oriented toward the ridge axis in some regions. However, these bands do not form at consistently low angles to the direction of maximum compression. This is attributed to the range in anisotropy magnitude throughout the MOR domain.

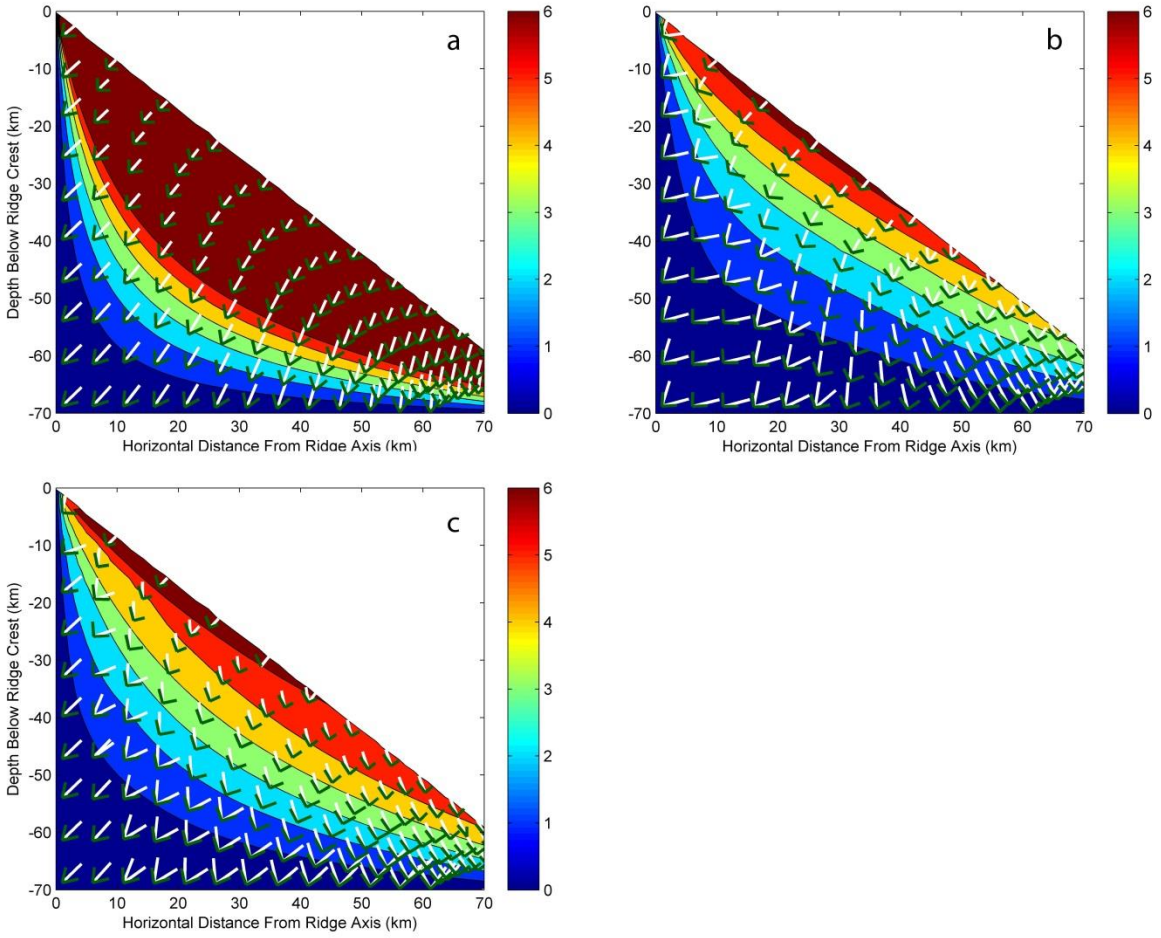

Figure 4: Contour plots of maximum perturbation amplitude with corresponding evolved orientations given in white, in some points showing two maxima. Shown in green are the half-maximum amplitude envelope orientations. These are included to account for broad, single peak maxima in some locations. a) All isotropic strain-rate independent bands have been rotated by the background flow leading to a more direct orientation toward the base of the plate. Significant regions of the MOR domain have a maximum perturbation amplitude that exceeds the limit of s_{max}. This leads to unphysical porosities and invalidates the linear analysis in that area for the case where $\Delta\phi = 0.1\phi_0$. b) Isotropic strain-rate dependent bands have undergone rotation, leading to most bands being oriented toward the base of the plate. c) Similarly, in the case of anisotropic strain-rate independent viscosity, rotation by the background flow has led to many bands being oriented toward the base of the plate.